

Lagrangian and geometric analysis of finite-time Euler singularities

T. Grafke^a, R. Grauer^a

^a*Institut für Theoretische Physik I, Ruhr-Universität Bochum, Germany*

Abstract

We present a numerical method of analyzing possibly singular incompressible 3D Euler flows using massively parallel high-resolution adaptively refined numerical simulations up to 8192^3 mesh points. Geometrical properties of Lagrangian vortex line segments are used in combination with analytical non-blowup criteria by Deng et al [Commun. PDE **31** (2006)] to reliably distinguish between singular and near-singular flow evolution. We then apply the presented technique to a class of high-symmetry initial conditions and present numerical evidence against the formation of a finite-time singularity in this case.

Keywords: Euler equation, Existence, uniqueness and regularity theory, Vortex line geometry, Adaptive mesh refinement

1. Introduction

For now more than two centuries, the incompressible Navier-Stokes equations have withstood the minds of mathematicians and physicists alike: The derivation of the nature of turbulence from the equations, as well as the global existence of smooth solutions is not known to date. The huge mathematical difficulties concerning the latter problem were recognized by its elevation to the status of “Millennium Prize Problem” by the Clay Mathematics Institute (see the official problem description by Fefferman [1], or review articles e.g. [2, 3]). A proof of existence of global regular solutions to the Navier-Stokes equation is believed to entail the development of completely new methods for the analysis of partial differential equations. The absence of mathematical certainty for the Navier-Stokes equations may seem to leave the physicist in a somewhat embarrassing position: The equation is known and well tested in application, but the existence of solutions is unclear in relevant cases.

Yet, the actual impact of a supposed breakdown of solutions for the Navier-Stokes equations on physics of fluids is smaller than one might expect and appears like a mere technical detail on second thought. Singularities in the

Email addresses: tg@tp1.rub.de (T. Grafke), grauer@tp1.rub.de (R. Grauer)

Navier-Stokes equation would, if existent, appear on very small scales. Obviously, continuum mechanics do not hold on these smallest scales and the breakdown of the model equation would appear in a regime in which the model does not describe reality at any rate. Furthermore, the nature of supposed singularities for the Navier-Stokes equation is proven to be unphysical in nature, as it requires the existence of infinite momentum. Without external forcing, from smooth initial conditions and in the presence of friction, the occurrence of infinite momentum is impossible to justify physically. The impact of singularities is additionally limited by the fact that the space-time dimension of the singular region is proven to be less than or equal to one for the Navier-Stokes equations [4].

In the inviscid limit, the situation is quite the opposite. The incompressible Euler equations for ideal fluids,

$$\frac{\partial \mathbf{u}}{\partial t} + \mathbf{u} \cdot \nabla \mathbf{u} + \nabla p = 0, \quad \nabla \cdot \mathbf{u} = 0. \quad (1)$$

appear to be of little physical significance in most applications, since friction is the dominating process on small scales. The ignorance regarding existence of global solutions is even larger for the inviscid case: The notion of weak solutions, which are well established for the Navier-Stokes equations since Leray [5], is unknown for the three-dimensional Euler equations. Nevertheless, the formation of finite-time Euler singularities significantly concerns our understanding of (viscid) fluid dynamics. Euler singularities, if existent, would coincide with the development of large gradients in the velocity field. Since no friction is limiting the increase in velocity gradients, infinite momentum is not mandatory for a blowup of the Euler equations. The inviscid limit is, therefore, not only a mere description of ideal fluids, but explores the possibility of inherent dynamical processes beyond friction that limit the transition to smaller and smaller scales. This has immediate implications on the existence of a cut-off velocity in high Reynolds-number Navier-Stokes flows, leading to the slightly exaggerated question, quoting Constantin [6]: “Do we need Schrödinger’s equations to calculate the flow around a moving car? Or to predict tomorrow’s weather?” For that reason, the problem of singularities for the Euler equations is of far greater importance to the physical understanding of fluids than the analogous problem for the Navier-Stokes equations.

A similar argument is valid for turbulence. Today’s phenomenological description of turbulence (e.g. [7, 8]), which is built on the basis of the celebrated theory by Kolmogorov [9–11], contains as a central point that, in the limit of vanishing viscosity, energy dissipation has to stay finite. This behavior could be explained by the formation of finite-time Euler singularities, as implied by Onsager’s conjecture [12]. For three-dimensional incompressible flow, non-conservation of energy might be caused not only by viscosity but by missing regularity in the velocity field. Energy dissipation might occur, if the Hölder continuity exponent is smaller than 1/3 for the velocity field. This conjecture was proven in terms of Besov spaces [13, 14]. As a consequence, a mathematical description of turbulence might be possible in terms of weak solutions for

the Euler equations, if smooth solutions gain enough roughness in finite time. Therefore, insight into the formation of finite-time singularities for the Euler equations could uncover a mechanism essential for the understanding of viscous turbulence.

The search for finite-time singularities of the Euler equations has resulted in extensive literature, with many analytical results being relatively young. Especially the advent of scientific computing has given research a new direction: Reports of numerical evidence supporting or denying the existence of finite-time singularities for the Euler equations are numerous (see e.g. [15] for a compiled list).

As a now classical result, the blowup criterion of Beale et. al [16] (BKM) connects the existence of solutions for the incompressible Euler equations in three dimensions to the critical accumulation of vorticity. More recently, geometric analysis of the flow [17, 18] has helped increasing insight into the process of vorticity growth. Among these geometric blowup criteria, theorems developed by Deng et. al [19] may be seen as the first to be suitable for verification by direct numerical simulations. An approach along this way will be presented in this paper.

Given the results of analytical considerations and the experience gained from numerical simulation of the Euler equations, certain scenarios are known to be possibly compatible with the analytic requirements of a finite-time blowup, namely the global notion of self-similar collapse to a point and the local process of vorticity accumulation by vorticity-strain coupling. It has been tried in the past to construct explicit initial conditions exploiting these scenarios to obtain numerical evidence for or against a finite-time singularity, with surprisingly inconsistent results. The major reason for this ambiguity is the critical dependence on extrapolation, which renders the identification of singular versus near-singular behavior next to impossible by numerical means. The hopes are high that the situation is less vague when considering geometric properties of the flow, as mentioned above. We will present the application of such geometric criteria to numerical data to sharpen the distinction between singular and near-singular flow evolution and identify the processes connected with this behavior.

This paper is organized as follows: we first review the relevant geometric blowup-criteria that form the basis of our numeric method. This includes a motivation of how geometric properties such as curvature or spreading of Lagrangian vortex line segments are connected to the accumulation of vorticity. We then describe the special class of high symmetry initial conditions used for our numerical experiments, discuss the implications of flow symmetries on the process of vorticity-strain coupling and introduce different vorticity profiles for vortex dodecapole initial conditions. Using this setup, details of the its implementation for our massively parallel simulations with up to 8192^3 mesh points are given. Results are presented concerning the growth of vorticity and strain, the BKM-criterion and the geometric criteria. These findings act as numerical evidence against the formation of a finite-time singularity for this class of initial conditions. A conclusion and outlook summarize the paper.

2. Geometric blowup criteria

Classical criteria for the development of a finite-time Euler singularity have in common that they focus on global features (such as certain norms of the velocity or the vorticity fields) or on point-wise Eulerian features (such as $\Omega(t)$) of the flow. This comes at the disadvantage of neglecting the structures and physical mechanisms of the flow evolution. A strategy to overcome such shortcomings was established by focusing more on geometrical properties and flow structures, such as vortex tubes or vortex lines. Starting with the works of Constantin et al. [17, 20] and Cordoba and Fefferman [18], some of these “geometric” criteria (e.g. [19, 21, 22]) have reached a phase where they allow direct verification of their assumptions with the help of numerical simulations. Special focus is placed on the criteria presented by Deng, Hou and Yu [19, 23], as the assumptions are in close reach for numerical simulations. They examine the Lagrangian evolution of vortex line segments and formulate a combined bound on velocity blowup and vortex segment collapse.

One of the trivial consequences of the BKM theorem is the fact that no blowup can occur for the two dimensional Euler equations. Since the vorticity $\omega(\mathbf{x}, t)$ is bounded by the initial conditions $\|\omega_0\|_{L^\infty}$ for all times, a critical accumulation is impossible. This is a direct consequence of the vorticity pointing out of the plane of motion, therefore having the vortex-stretching term $\omega \cdot \nabla \mathbf{u}$ vanish everywhere. This may be interpreted as a motivation to focus on the behavior of the direction of vorticity, $\xi = \omega/|\omega|$ in the three-dimensional case. For 2D, ξ is a constant in space and time (neglecting sign). In 3D, the consequences of the regularity of ξ on the growth-rate of vorticity and ultimately of the applicability of BKM can be precisely stated.

For the Euler equations, this was introduced by Constantin et al. [17]. They state, roughly, that for a smoothly directed vorticity in an $O(1)$ -region there may be no blowup in finite time as long as the velocity remains finite in this region. Even though this criterion takes into account the local structure of the flow and follows the evolution of vortex lines, the (global) bound on the velocity makes this theorem hard to apply in practice. Numerical simulations of the Euler equations give no evidence for the velocity to be uniformly bounded in time. This restriction on the velocity field is weakened in a similar criterion by Cordoba and Fefferman [18]. They consider vortex tubes with some properties concerning their regularity and a surrounding $O(1)$ region Q of the flow. From this it is possible to deduce, with the help of a milder assumption on the surrounding velocity, that the vortex tube cannot reach zero thickness in finite time. Even though the velocity field is no longer required to be uniformly bounded in time, the notion of “regular tube” of $O(1)$ length is too restricting, compared to the experiences of numerical simulations.

2.1. Regularity of vorticity direction along a vortex line

Vortex lines of the three-dimensional incompressible Euler equations, defined as integral curves of the vorticity direction field, are transported with the flow. As a consequence, two points \mathbf{x} and \mathbf{y} on the same vortex line $c(s)$ stay on

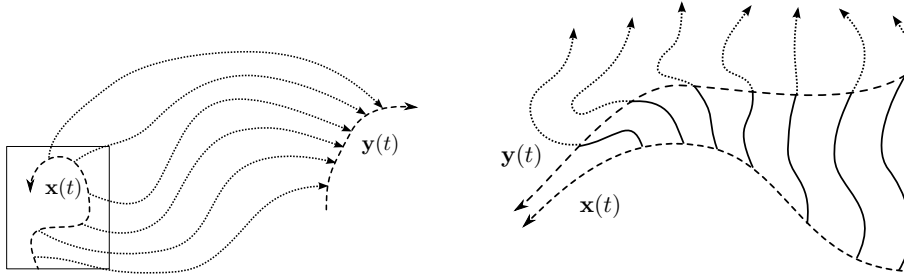


Figure 1: Two ways to apply theorem 1. Left: Choose $\mathbf{y}(t)$ such that it is far outside of the critical region of maximum vorticity and monitor the behavior of $\int_{\mathbf{x}(t)}^{\mathbf{y}(t)} (\nabla \cdot \boldsymbol{\xi})(c(s), t) ds$. Right: For the position $\mathbf{x}(t)$ of maximum vorticity, choose $\mathbf{y}(t)$ such that $\int_{\mathbf{x}(t)}^{\mathbf{y}(t)} (\nabla \cdot \boldsymbol{\xi})(c(s), t) ds = C$. For a point-wise singularity, $\mathbf{x}(t)$ and $\mathbf{y}(t)$ must collapse in finite time.

the same vortex line for all times. Furthermore, as a direct implication of the solenoidality of the vorticity vector field, the vorticity flux through a vortex tube is the same for each cross-section.

These two arguments may be combined to get a differential notion of the connection between the vorticity at two different points on the same vortex line. A simple consequence of the solenoidality of $\boldsymbol{\omega}$ results in

$$(\boldsymbol{\xi} \cdot \nabla)|\boldsymbol{\omega}| = -|\boldsymbol{\omega}|(\nabla \cdot \boldsymbol{\xi}) . \quad (2)$$

Since for a vortex line $c(s)$ it holds by definition that $\dot{c}(s) = \boldsymbol{\xi}(c(s))$, we have $\boldsymbol{\xi} \cdot \nabla \equiv \partial/\partial s$, where $\partial/\partial s$ is the partial derivative in direction of the vortex line. Thus, integrating eq. (2) along the vortex line yields

$$|\boldsymbol{\omega}(\mathbf{y}(t), t)| = |\boldsymbol{\omega}(\mathbf{x}(t), t)| \exp \left(- \int_{\mathbf{x}(t)}^{\mathbf{y}(t)} \nabla \cdot \boldsymbol{\xi} ds \right) . \quad (3)$$

Paraphrased, this means: The vorticity at two different points on the same vortex line is connected by the amount of converging or diverging of neighboring vortex lines along their interconnecting path. The more violent vortex lines converge around a vortex line, the faster the vorticity grows along that line.

This finding was connected with BKM by Deng et al. [19] to formulate a geometric blowup criterion. It is obvious from equation (3) that the maximum vorticity $\Omega(t)$ at a given time t can be estimated by the vorticity on its vortex line, as long as $\nabla \cdot \boldsymbol{\xi}$ remains finite. In detail this means:

Deng-Hou-Yu theorem 1: *Let $\mathbf{x}(t)$ be a family of points such that for some $c_0 > 0$ it holds $|\boldsymbol{\omega}(\mathbf{x}(t), t)| > c_0 \Omega(t)$. Assume that for all $t \in [0, T)$ there is another point $\mathbf{y}(t)$ on the same vortex line as $\mathbf{x}(t)$, such that the direction of vorticity $\boldsymbol{\xi}(\mathbf{x}, t) = \boldsymbol{\omega}(\mathbf{x}, t)/|\boldsymbol{\omega}(\mathbf{x}, t)|$ along the vortex line $c(s)$ between $\mathbf{x}(t)$ and $\mathbf{y}(t)$ is well-defined. If we further assume that*

$$\left| \int_{\mathbf{x}(t)}^{\mathbf{y}(t)} (\nabla \cdot \boldsymbol{\xi})(c(s), t) ds \right| \leq C \quad (4)$$

for some absolute constant C , and

$$\int_0^T |\omega(\mathbf{y}(t), t)| dt < \infty, \quad (5)$$

then there will be no blowup up to time T .

It is immediately clear how this criterion can be applied to numerical simulations: If the maximum vorticity $\Omega(t)$ exhibits fast growth in time for which it is hard to decide whether it is a finite-time blowup compatible with BKM, instead one could monitor the vorticity outside the critical region, but on the same vortex line. If it remains well bounded, and $\nabla \cdot \boldsymbol{\xi}$ along the vortex line does not scale critically in time, it is safe to deduce a non-critical growth of $\Omega(t)$. This approach is sketched in Fig. 1 (left).

However, due to the freedom of the choice of $\mathbf{y}(t)$ on the critical vortex line, theorem 1 may be employed in a different way to distinguish different scenarios for a finite-time singularity, as depicted in Fig. 1 (right). Suppose that the maximum vorticity $\Omega(t)$ grows in a way compatible with BKM. Now, choose $\mathbf{x}(t)$ to be the position of maximum vorticity and define $\mathbf{y}(t)$ via

$$\int_{\mathbf{x}(t)}^{\mathbf{y}(t)} \nabla \cdot \boldsymbol{\xi} ds = C \quad (6)$$

for some constant C independent of the time t , where s denotes the arc-length parameter of the curve from $\mathbf{x}(t)$ to $\mathbf{y}(t)$. In words, choose $\mathbf{y}(t)$ on the same vortex line as $\mathbf{x}(t)$ such that the accumulation of tightening of nearby vortex lines is the same for every instance in time. This provides us with the ability to clearly distinguish between to separate cases of supposed blowup:

- (i) For every constant C , $\mathbf{y}(t)$ approaches $\mathbf{x}(t)$ in finite time to collapse to a single point. This would constitute the desired behavior for a point-wise singularity in the origin.
- (ii) If for any constant C , $\mathbf{x}(t)$ and $\mathbf{y}(t)$ stay well separated in time and do not collapse to a point, the whole vortex-line from $\mathbf{x}(t)$ to $\mathbf{y}(t)$ has to blow up in order to maintain critical growth in $\mathbf{x}(t)$. This scenario, however unlikely, is not ruled out analytically.

The insight provided by the theorem could successfully be used as evidence excluding a point-wise singularity for the considered initial conditions as presented below.

2.2. Vortex line stretching and vorticity accumulation

Vortex stretching is recognized as the mechanism responsible for the accumulation of vorticity. Revisited from a geometric point of view, vortex lines are transported with the flow, yet twist and turn due to vortex stretching. Since in the absence of dissipation vortex lines are unable to reconnect, the topological properties of vortex lines are fixed. A complex flow will therefore entangle, stretch and twist vortex lines in a non-trivial way.

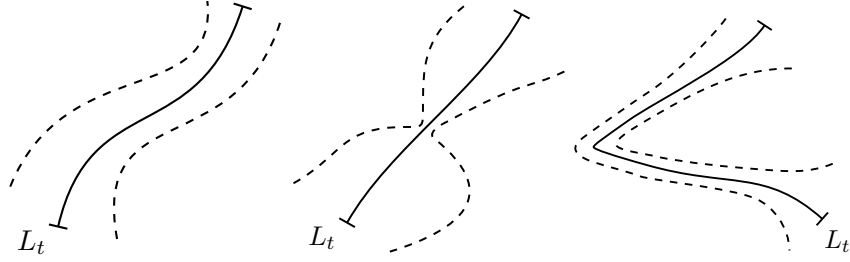


Figure 2: Characterizing vortex line geometry in terms of $\lambda(L_t)$. A slightly curved vortex line with approximately parallel neighboring vortex lines (left) exhibits small $\lambda(L_t)$. Vortex lines with tightening neighboring vortex lines (center) or vortex lines with high curvature, in comparison to their length (right) have high $\lambda(L_t)$.

The geometric equivalent of the vortex stretching term is the increase in length for a Lagrangian vortex line. It is possible to quantify this stretching and establish a sound connection to the vorticity dynamics of the flow. This in turn can then be used to reformulate blowup criteria in terms of geometric constraints on Lagrangian vortex lines. This section is meant to give an overview over this procedure to understand the implications of the second theorem of [19]. Details regarding the statements below are given therein.

Consider a vortex line segment L_0 at time $t = 0$ and its Lagrangian image $L_t = \mathbf{X}(L_0, t)$. Let β, s be the arc length parameters of L_t at times 0 and t . Then, a direct implication of the vorticity transport formula describes the evolution of the absolute vorticity at a Lagrangian fluid element

$$|\boldsymbol{\omega}(\mathbf{X}(\alpha, t), t)| = \boldsymbol{\xi}(\mathbf{X}(\alpha, t), t) \cdot \nabla_{\alpha} \mathbf{X}(\alpha, t) \cdot \boldsymbol{\xi}_0(\alpha) |\boldsymbol{\omega}_0(\alpha)| \quad (7)$$

$$= \frac{\partial s}{\partial \beta} |\boldsymbol{\omega}_0(\alpha)|, \quad (8)$$

meaning that the local stretching of the length of a vortex line segment that is transported with the flow is equivalent to the growth of vorticity at the corresponding transported fluid element.

This result can be transformed into a bound for the length of a vortex line by the vorticity along this line. Denote with $l(t)$ the length of the vortex line segment L_t at time t and define with

$$\Omega_L(t) := \|\boldsymbol{\omega}(\cdot, t)\|_{L^{\infty}(L_t)} \quad (9)$$

the maximum vorticity on the vortex line segment. Furthermore, let

$$M(t) := \max(\|\nabla \cdot \boldsymbol{\xi}\|_{L^{\infty}(L_t)}, \|\kappa\|_{L^{\infty}(L_t)}) \quad (10)$$

be the quantity of vortex line convergence $\nabla \cdot \boldsymbol{\xi}$ and vortex line curvature κ , and define $\lambda(L_t) := M(t)l(t)$. Then, the relative increase of the length of the vortex line segment in a time interval, $l(t)/l(0)$, is bounded as

$$e^{-\lambda(L_t)} \frac{\Omega_l(t)}{\Omega_l(0)} \leq \frac{l(t)}{l(0)} \leq e^{\lambda(L_0)} \frac{\Omega_l(t)}{\Omega_l(0)}. \quad (11)$$

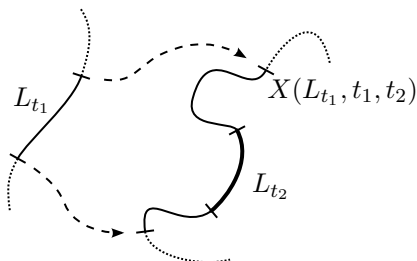


Figure 3: Visualization of the evolution of a vortex line segment in theorem 2: At a late time $t_2 > t_1$ the segment L_{t_2} has to be included in the Lagrangian evolution of L_{t_1} , but is free to be just a fraction of it.

This result, which is a slight modification of a lemma in [19], may be viewed in its own right: The relative increase in length along a time-interval is bounded by the vorticity increase and a factor $\exp(\pm\lambda(L_t))$. Thus, $\lambda(L_t)$ is a dimensionless number, characterizing the geometric “tameness” of the vortex line filament.

As depicted in Fig. 2, a vortex line segment has a huge $\lambda(L_t)$, if its maximum curvature is large, relative to its length (the segment is “kinked” instead of “curved”), or if the surrounding vortex lines collapse to the considered segment in at least a point (the surrounding is “tightening” instead of “parallel”). A relatively unbent vortex line segment with approximately parallel neighboring vortex lines possesses a low value of $\lambda(L_t)$. This quantifies the constricted notion of “relatively straight” and “smoothly directed” given in [17] in a sharper way.

2.3. Lagrangian evolution of vortex line segments

Connecting the stretching process stated above with the Lagrangian accumulation of vorticity,

$$\frac{D}{Dt}|\boldsymbol{\omega}| = [(S\xi) \cdot \xi]|\boldsymbol{\omega}|, \quad (12)$$

where $S = 1/2(\nabla\mathbf{u} + \nabla\mathbf{u}^T)$ is the strain tensor, and noting that the *curvature* κ of the vortex line L_t fulfills

$$\kappa\mathbf{n} = \frac{\partial\dot{L}_t(s)}{\partial s} = \frac{\partial\xi}{\partial s} = (\xi \cdot \nabla)\xi, \quad (13)$$

with $\mathbf{n} = \ddot{L}_t/|\ddot{L}_t|$ being the unit normal vector of the vortex line, the Lagrangian evolution of vortex line stretching, by inserting eq. (8), becomes

$$\frac{D}{Dt}\left(\frac{\partial s}{\partial\beta}\right) = \frac{\partial}{\partial\beta}(\mathbf{u} \cdot \xi) - \kappa(\mathbf{u} \cdot \mathbf{n})\left(\frac{\partial s}{\partial\beta}\right). \quad (14)$$

At this point it becomes obvious how the process of vortex line stretching interacts with the velocity in two distinct ways: The velocity in direction of the vortex line elongates the segment by drawing it out, while a part of the velocity normal to the vortex line increases the segment’s length by enlarging its curves.

Integrating (14) along the vortex line (from β_1 to β_2) and over time (from 0 to t) results in

$$l(t) \leq l(0) + \int_0^t [U_\xi(\tau) + \lambda(\tau)U_n(\tau)] d\tau, \quad (15)$$

for

$$U_\xi(t) := \max_{\mathbf{x}, \mathbf{y} \in L_t} |(\mathbf{u} \cdot \boldsymbol{\xi})(\mathbf{x}, t) - (\mathbf{u} \cdot \boldsymbol{\xi})(\mathbf{y}, t)|$$

$$U_n(t) := \max_{L_t} |\mathbf{u} \cdot \mathbf{n}|$$

Instead of starting the above reasoning at time $t = 0$, the results are identical for a later time $0 < t_1 < t$. This result may be understood as an upper bound for vortex line stretching in terms of velocity and vortex line geometry. In conjunction with the connection between length increase and vorticity amplification, given in equation (11), one arrives at

$$\Omega_l(t) \leq \Omega_l(0)e^{\lambda(L_t)} \left[1 + \frac{1}{l(0)} \int_0^t (U_\xi(\tau) + \lambda(\tau)U_n(\tau)) d\tau \right].$$

This is an inequality for the control of growth rate of the vorticity by geometric flow properties. From this estimate, by combining it with BKM to distinguish critical from sub-critical vorticity growth, the central non-blowup criterion of [19] is derived:

Deng-Hou-Yu theorem 2: *Assume there is a family of vortex line segments L_t and $T_0 \in [0, T)$, such that $L_{t_2} \subseteq \mathbf{X}(L_{t_1}, t_1, t_2)$ for all $T_0 < t_1 < t_2 < T$. We also assume that $\Omega(t)$ is monotonically increasing and $\|\omega(t)\|_{L^\infty(L_t)} \geq c_0\Omega(t)$ for some $c_0 > 0$ when t is sufficiently close to T . Furthermore, we assume that*

- (i) $\lambda(L_t) \leq C_0$,
- (ii) $l(t) \gtrsim (T - t)^B$ for some $B \in (0, 1)$.
- (iii) $U_\xi(t) + U_n(t)\lambda(L_t) \lesssim (T - t)^{-A}$ for some $A < 1 - B$

Then there will be no blowup in the 3D incompressible Euler flow up to time T .

Here, $a(t) \lesssim b(t)$ means there exists a constant $c \in \mathbb{R}$ such that $|a(t)| < c|b(t)|$ (and accordingly for $a(t) \gtrsim b(t)$). The choice of Lagrangian vortex segments is sketched in Fig. 3.

It should be noted that theorem 2 again includes assumptions on the dimensionless number $\lambda(L_t)$. Especially assumption (i) poses a uniform bound in time for $\lambda(L_t)$. This translates to words as the process of “zooming in” to the location of maximum vorticity in order to keep the considered vortex line segment relatively straight in comparison to its length. The assumed accompanying collapse in length to keep $\lambda(L_t)$ bounded is then linked in its growth rate to the blowup of the velocity components.

It is worth mentioning that the above presented criterion, even though it is obviously inspired by the classical geometric criteria, still differs in crucial

aspects. The posed assumptions are purely local and restricted to the geometry of a single critical vortex line filament. Assumptions on the velocity do not, in contrast to Constantin et al. [17], impose a uniform bound (which is not observed in simulations), but allow for a finite-time blowup of velocity, strictly connected in its growth rate to the geometrical evolution of the filament. The vortex line segment itself is not assumed to be of $O(1)$ length (as in [18]) or to be contained in an $O(1)$ -region (which, again, was not observed in simulations). These aspects in combination render it a promising theorem to be directly tested by numerical simulations.

2.4. Scenarios for finite-time singularities

It has been established that a singularity of the Euler equations in finite time necessitates rapid accumulation of vorticity. Locally, vorticity-strain coupling is identified as the mechanism for nonlinear amplification in finite time. Globally, the notion and possibility of self-similar or locally self-similar collapse to a point is introduced. These aspects serve as a basis for the construction of initial conditions suitable for the possible formation of a finite-time singularity.

Due to the incompressibility condition, the trace of S vanishes and due to the symmetry of S its eigenvalues λ_i are real and the corresponding eigenvectors \mathbf{v}_i are orthogonal. Thus λ_1 , the biggest eigenvalue, fulfills $\lambda_1 > 0$ in regions with non-vanishing strain. As a direct consequence of equation (12), if λ_1 is proportional to the vorticity in direction \mathbf{v}_i then the vorticity growth would be compatible with a finite-time singularity according to BKM. This coupling of the strain to the vorticity is crucial. If the strain rate is constant instead, the growth in vorticity is merely exponential. Several cases have been suggested in which this mechanism of coupling may take place.

It should be noted that, contrary to expectations, the vorticity-strain coupling does not readily appear in nature. One would expect a tendency of the vorticity to align itself to the eigenvector of the strain tensor with the largest eigenvalue all by itself, since the parallel component is amplified, while the orthogonal components are damped or stay nearly constant. Nevertheless, for viscid turbulent flows, quite a different behavior is observed both in numerical simulations and experiments: The vorticity is most likely to align to the intermediate eigenvector of the strain tensor [24–26] and similarly for the Euler equation [27]. One can therefore expect that functional vorticity-strain coupling is inherently unstable. The process has to be designed “artificially” by choosing suitable initial conditions.

A more precise notion of the process of vorticity alignment in turbulent flows is given by Hamlington, Schumacher and Dahm [28]. They distinguish, evaluating the Biot-Savart law numerically, between strain induced *locally* by the immediate neighborhood and *globally* by long-range interaction. For turbulent flows, they observe a most likely alignment of the vorticity to the most positive eigenvector of the global strain. Taking into account also the local strain restores the alignment of vorticity to the intermediate eigenvector. Contrary to this, for the successful emergence of a finite-time singularity of the Euler equations in a point-wise sense, vorticity-strain coupling should be induced by the local strain

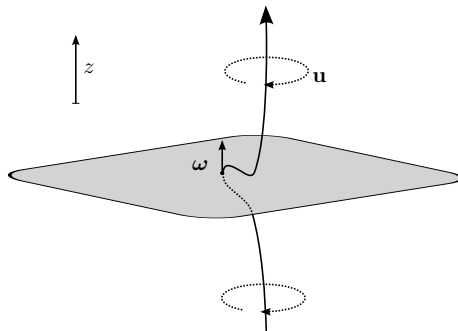


Figure 4: Effects of planes of reflectional symmetry on intersecting vortex tubes: In the symmetry plane, the vorticity ω is normal and the strain tensor possesses a parallel eigenvector with corresponding eigenvalue S_{zz} . The curvature κ in the symmetry plane has to increase in order to support critical vorticity-strain coupling.

to support a collapse to a point. A numerical application of this technique from [28] to Euler blowup simulations will be presented elsewhere.

3. Initial conditions

Different initial conditions were introduced and subsequently improved or refined to construct flows with prolonged intervals of vorticity-strain coupling, and it seems natural to search for techniques to artificially keep the coupling existent. One such technique is the introduction of symmetries to the flow. Early examples such as the Taylor-Green vortex [29] or Kerr's initial conditions [30–32] are employing such symmetries.

3.1. Reflectional symmetries

Consider the plane $z = 0$ to be a plane of reflectional symmetry, as shown in Fig. 4, defined by

$$\begin{aligned} u_x(x, y, z) &= u_x(x, y, -z) \\ u_y(x, y, z) &= u_y(x, y, -z) \\ u_z(x, y, z) &= -u_z(x, y, -z) \end{aligned}$$

for the velocity vector field, which leads to $u_z = 0$ in the plane of symmetry. Accordingly, the vorticity obeys

$$\begin{aligned} \omega_x(x, y, z) &= -\omega_x(x, y, -z) \\ \omega_y(x, y, z) &= -\omega_y(x, y, -z) \\ \omega_z(x, y, z) &= \omega_z(x, y, -z) \end{aligned}$$

and in particular $\omega_x = \omega_y = 0$ or $\boldsymbol{\omega} = \omega_z \hat{e}_z$ in the plane of symmetry. Due to these properties, the strain tensor has $S_{xz} = S_{yz} = S_{zx} = S_{zy} = 0$, or

$$S = \begin{pmatrix} S_{xx} & S_{xy} & 0 \\ S_{xy} & S_{yy} & 0 \\ 0 & 0 & S_{zz} \end{pmatrix}. \quad (16)$$

It immediately follows that the eigenvector corresponding to the eigenvalue S_{zz} is directed normally to the symmetry plane, and the vorticity vector is aligned to it. Note that this is the sole consequence of the reflectional symmetry and is in no way influenced by the flow. A vortex tube normal to the symmetry plane therefore seems like a natural candidate for critical accumulation of vorticity by means of vorticity-strain coupling: All that is needed is a sufficiently long period of time in which $S_{zz} \sim \omega_z$ at one point of the symmetry plane.

This possibility has been analyzed by Pelz [33]: Taking into account only the zz -component, the strain tensor in the plane of symmetry is given by the Biot-Savart law as

$$S_{zz} = \frac{3}{4\pi} \int ((x - x')\omega_y(\mathbf{x}') - (y - y')\omega_x(\mathbf{x}')) \frac{(z - z')}{|\mathbf{x} - \mathbf{x}'|^5} d\mathbf{x}'. \quad (17)$$

Equation (17) shows that S_{zz} in the plane of symmetry does not scale with ω_z , but does instead depend on ω_x and ω_y , which are both equal to zero in the $z = 0$ plane. Yet, in close proximity to the plane, ω_x and ω_y may grow, depending on the curvature of the vortex line intersecting the symmetry plane: A Taylor expansion around the $z = 0$ plane yields:

$$\omega_i = h \left. \frac{\partial \omega_i}{\partial z} \right|_{z=0} = h \kappa_i \omega_z(z = 0)$$

for small h up to first order, for $\kappa_i = \kappa \mathbf{n}_i$. Therefore, if the curvature is huge close to the plane of symmetry, ω_i with $i \in \{x, y\}$ approximately scales like ω_z and thus S_{zz} may scale with ω_z too. However, for this to happen, we need $\kappa \approx 1/h$. As a matter of fact, the dimensionless number $\kappa_i h$ plays a similar role as the characteristic geometric number $\lambda(t)$ introduced in section 2.2. For S_{zz} to blow up like ω_z , the curvature has to increase in a way to counter the shrinking of the length scale h .

On the other hand, the axial strain S_{zz} stretches the vortex tube in z -direction. This counteracts any increase in curvature to a certain degree. More precisely, the Lagrangian evolution of the curvature components κ_x and κ_y were calculated in [33]:

$$\begin{aligned} \frac{D}{Dt} \kappa_x &= (S_{xx} - 2S_{zz})\kappa_x + S_{yy}\kappa_y + \partial_z S_{yz} \\ \frac{D}{Dt} \kappa_y &= S_{xx}\kappa_x + (S_{yy} - 2S_{zz})\kappa_y + \partial_z S_{xz}. \end{aligned}$$

The axial strain S_{zz} diminishes both κ_x and κ_y .

These counteracting processes of vortex line geometry are by no means analytically exact, since all long-range interactions have been ignored. Nevertheless, they constitute an intrinsic resistance of a single vortex line to “self-stretch” in a critical way. The argument may be readily translated to the case of (perturbed) anti-parallel vortex tubes: Since no other components of vorticity are introduced, S_{zz} still only depends on ω_x and ω_y which in turn rely on high curvature to scale like ω_z close to the plane of symmetry.

One way to counter this is to induce the axial strain by neighboring tubes instead of relying on a sufficiently large kink. This will be presented in the following section by introducing additional rotational symmetry.

3.2. High symmetry initial conditions

One notable high-symmetry flow was introduced by Kida [34] and has subsequently been used extensively to probe a possible Euler blowup numerically [35–37] or analytically (e.g. [38]) as well as study the onset of turbulence (e.g. [39]). The Kida-Pelz flow has a three-fold rotational symmetry about the diagonal and a reflectional symmetry about all three Cartesian planes. Flows with these two properties are termed as invariant under the full octahedral group [33]. The Euler (and Navier-Stokes) equations preserve the Kida-Pelz symmetries. In general one can write these initial conditions as

$$v(x, y, z) = \sum_{l,m,n} a_{lmn} \sin(lx) \cos(my) \cos(nz) \quad (18)$$

$$\mathbf{u} = (u_x, u_y, u_z)^T = (v(x, y, z), v(y, z, x), v(z, x, y)) . \quad (19)$$

This means, for a computational domain spanning the interval $[0, \pi]$ in all three dimensions, that the normal component of the velocity field is anti-symmetric under reflection at the Cartesian planes while the tangential components are symmetric. Combining this with the three-fold rotational symmetry adds up to a total memory saving factor of 1/24.

On the same time there is reason to hope that these rather artificial symmetries encourage singular behavior if the initial conditions are constructed accordingly. When assuming a localized vortex tube intersecting the symmetry plane normally, as depicted in Fig. 5, its mirror images result in a total of six pairs of anti-parallel vortex tubes. It has been proposed by Pelz [33] that the strain induced by the rotational images of each tube, assuming a velocity field supporting a collapse to the origin, may lead to the desired vorticity-strain coupling without being subject to the counteraction of strain and curvature in the planes of symmetry. Provided that the vortex dodecapole retains its shape during collapse, this scenario could lead to a finite-time collapse to the origin.

3.2.1. Vortex dodecapole initial conditions

One form of these initial conditions is based on the idea to already start with six dipoles consisting of vortices of a designated vorticity profile. An example

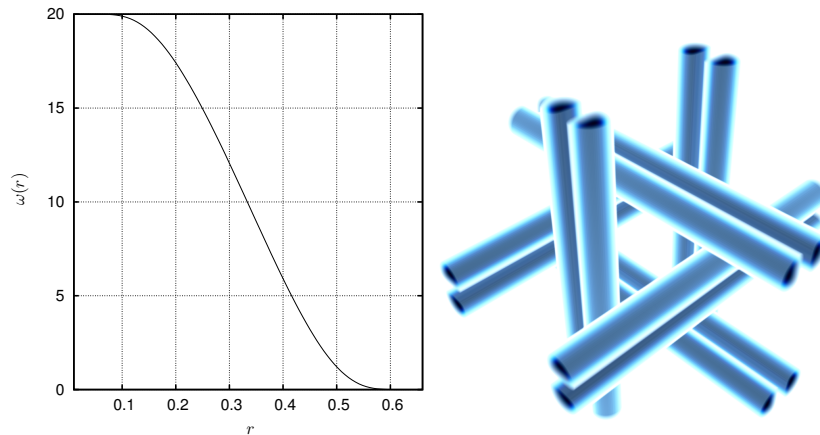


Figure 5: Left: Vorticity profile of one tube of the 12-tube initial condition (with $A = 20$). Right: Volume plot of the vorticity for the whole domain.

is the vortex dodecapole initial condition [40] with a vorticity profile given by

$$\omega(r) = \begin{cases} -A \left[1 - \exp \left(-e^2 \log(2) \frac{1}{3r} \exp \left(\frac{1}{\frac{3r}{2} - 1} \right) \right) \right] & \text{for } r < \frac{2}{3} \\ 0 & \text{for } r \geq \frac{2}{3} \end{cases} \quad (20)$$

where r denotes the distance to the tube's center line. The vorticity decreases with increasing distance to the center line and is strictly zero for $r > 2/3$. Thus, the vortex has compact support in the r - φ -plane while still being smooth. Fig. 5 (left) displays the vorticity profile given above, Fig. 5 (right) shows the whole dodecapole. Only one octant, i.e. three vortices, are simulated due to symmetry. For the reasons lined out in the previous sections, this kind of dodecapole appears to very promising in terms of developing a finite-time singularity in the origin because of reciprocal strain of the mirror tubes. It is furthermore susceptible to the analysis by the presented geometric blowup criteria. Most of the diagnostics in this paper are therefore performed on flows which are based on initial conditions of this type.

3.2.2. Lamb-dodecapole initial conditions

For the Euler equations, a single stretch-free axisymmetric vortex may have *arbitrary* radial dependence for the vorticity to remain stationary in time. The same is not true for vortex dipoles: An isolated vortex dipole propagating through the domain does not preserve its shape. This so-called *vortex shedding* is believed to influence and possibly suppress a self-amplifying behavior [41].

There are exact form-preserving dipole solutions of the 2-dimensional Euler equations which may be used to construct initial conditions that do not exhibit

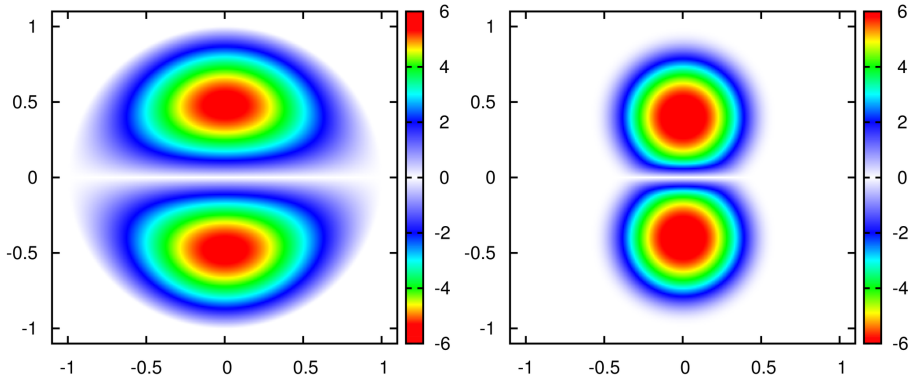


Figure 6: Comparison of vorticity profile for a Lamb dipole to the simple dipole. Left: Lamb dipole used in the Lamb-dodecapole initial conditions. Right: Dipole used in vortex dodecapole initial conditions. Both are scaled to fit in amplitude and size.

vortex shedding. The most famous is the Lamb-dipole introduced by Lamb [42]. Following [43] it is defined by

$$\omega(r) = \begin{cases} 2Uk \frac{J_1(kr)}{J_0(ka)} \sin(\theta) & \text{for } r < a \\ 0 & \text{for } r \geq 0 \end{cases} \quad (21)$$

where k is chosen such that ka is the first zero of J_1 , i.e. $ka \approx 3.8317$. In Fig. 6 this vorticity distribution is compared to the vorticity profile given in equation (20). Note that even though the distribution of vorticity for the Lamb dipole appears to be less sharp than for the simple profile, it is not differentiable at $r = a$, as can be seen in equation (21). Because of this, strictly speaking, the Lamb dipole is an improper candidate for the search for finite-time singularities. This issue is usually overcome by smoothing high frequency components in order to smear out the discontinuity in the gradient of the vorticity.

Orlandi and Carnevale [41] were the first to use Lamb dipoles to construct a colliding pair of dipoles, observing a rapid amplification of vorticity for a period of time, with a slowing growth at later times due to either depletion of nonlinearity [44] or lack of resolution. The Lamb dipole is used in a similar manner in the context of this paper to form a Lamb dodecapole analogous to vortex dodecapole initial conditions presented above.

4. Numerical experiment

Along the lines of the above presented mechanism for a finite-time singularity for the Euler equations, a number of numerical simulations were performed in the last decade to act as evidence for or against a blowup. Beginning in the early 80s of the last century, numerous numerical simulations with a variety of methods and schemes and differing initial conditions were tested, from Padé

approximants [45], vortex-segment methods [46, 47] and vortex filament models [48], to projection methods [49], pseudo spectral simulations [32, 37, 50, 51], Chebychev codes [30] and adaptive mesh refinement [27, 52]. Despite ever growing resolution, from 128^3 [49] up to 4096^3 mesh-points of adaptive simulations [40] or latest pseudo-spectral codes [53], results are often inconclusive or even conflicting.

In this paper The need for high resolution is met via massively parallel adaptive mesh refinement for the results presented. This high resolution data is then analyzed on the basis of the geometric blowup criteria presented in section 2.

4.1. Computational Framework

All numerical simulations throughout this work were conducted using the recently developed framework *racoona III* (refined adaptive computations with object-oriented numerics, based on [54]). Its key feature is the integration of partial differential equations on adaptive grids on massively parallel distributed computers. Most Euler blowup scenarios feature extremely localized structures with steep gradients, where a fixed mesh would under-resolve the crucial parts while wasting resources on the less important ones.

Adaptive mesh refinement increases the locally available resolution, but comes at the cost of additional computational overhead. It complicates the framework in several ways. Most importantly, it restricts the choice of numerical schemes to comparatively simple low order finite difference or finite volume variants. A direct comparison to high accuracy pseudo-spectral simulation was made in [40] for the case of Euler equations. It was found that a resolution approximately 1.3 times higher is needed to reach a comparable accuracy for the adaptively refined code.

To decide which regions are to be refined, the norm of the gradient of velocity, $\|\nabla \mathbf{u}(\mathbf{x}, t)\|$ is compared to a threshold. If the block is flagged as being under-resolved, it is bisected into 2^d child blocks that are redistributed among the available nodes. The resolution of the parent block is thus effectively doubled. The opposite happens for blocks that are over-resolved: 2^d blocks are merged into one, the resolution at this location is halved. With this procedure, the grid is constantly changing and adapting to the simulation, as shown in Fig. 7, allowing high resolution at critical locations but not wasting any resources for the rest.

Since communication between different nodes is the smallest bottleneck due to limited bandwidth and high latency, it is advantageous to arrange the blocks in a way that physically close blocks are located on the same node. Even if this seems to be pretty straight-forward for normal grids, it poses a larger problem for adaptive grids with different resolutions. In *racoona III*, blocks are distributed along a space-filling Hilbert curve, as sketched in Fig. 8.

This ensures that proximate blocks are located on the same node even if the grid is not fixed. Currently *racoona III* uses a slightly different approach, using independent Hilbert curves for each level, since inter-level communication

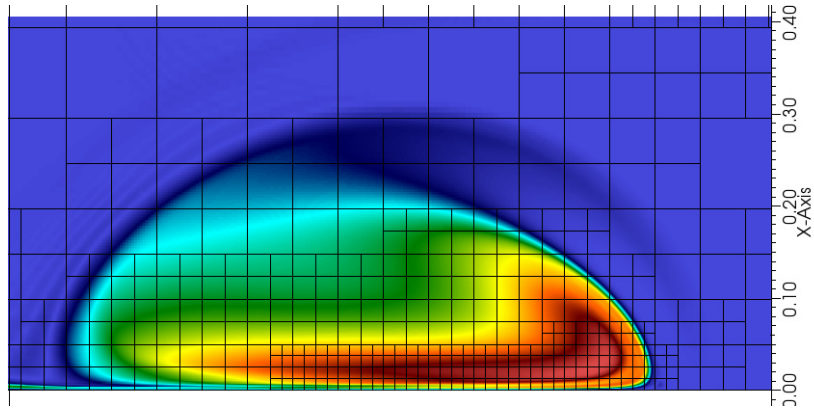


Figure 7: Refinement criterion for the simulation of the Euler equations with *racoon III*. Regions with a large value for $\|\nabla \mathbf{u}\|$ are resolved higher. Each square represents a block with 16^3 cells. Shown is the absolute vorticity for a cross-section of one vortex tube.

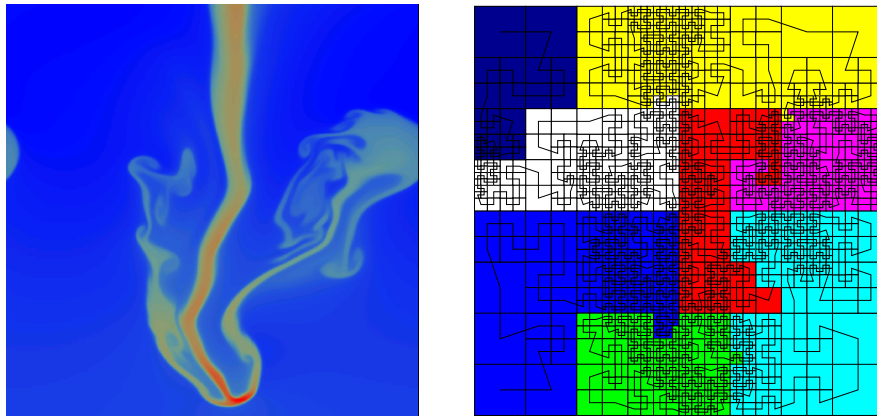


Figure 8: Adaptive mesh refinement and dynamic load balancing. The workload is distributed among different processors along a space-filling Hilbert curve.

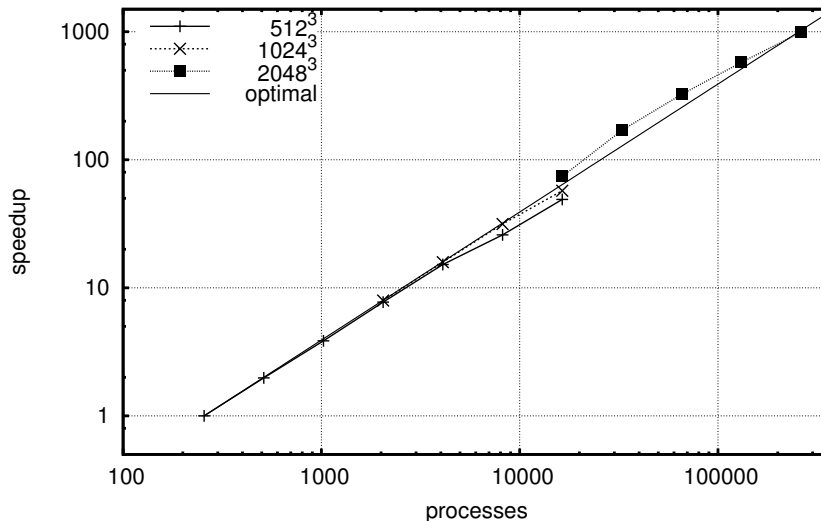


Figure 9: Mixed weak and hard scaling for the framework *racoon* for a hyperbolic test problem. The scaling is close to linear for up to 262144 cores.

is the most frequent type of communication for common problems. Every time the grid changes when adapting to the current situation, the Hilbert curve is recalculated, as is the workload for each node. If an imbalance is detected, the blocks are redistributed along the curve, each node getting roughly the same amount of blocks.

The numerical scheme consists of a strong stability preserving third order Runge-Kutta [55] time integrator combined with a third order shock-capturing CWENO scheme [56] to reduce oscillations in the presence of strong gradients. The integrated equation is the vorticity formulation of the Euler equations,

$$\frac{\partial}{\partial t} \boldsymbol{\omega} + \nabla \times (\nabla(\mathbf{u} \otimes \mathbf{u})) = 0, \quad (22)$$

employing a vector potential formulation $\Delta \mathbf{A} = -\boldsymbol{\omega}$ with $\mathbf{u} = \nabla \times \mathbf{A}$ to ensure solenoidality of the vorticity vector field $\boldsymbol{\omega}$. The associated Poisson equation is solved with a second order parallel and adaptive multigrid algorithm via a full approximation scheme to account for the non-uniform meshes, with flux correction at refinement interfaces. Interpolation on the coarse-fine interfaces is done in $\boldsymbol{\omega}$ for the whole scheme to ensure the highest possible accuracy in the critical variable. Passive tracer particles are injected into the flow for the tracking of Lagrangian vortex line segments. The above third order Runge-Kutta is also used for the time integration of the tracer particles and the space integration of vortex lines.

The overall scaling for *racoon* is depicted in Fig. 9 for a hyperbolic test problem (compressible MHD). It was measured on the BlueGene/P machine at

Forschungszentrum Jülich with a total number of 294912 cores. For a combination of weak and hard scaling, the performance is close to linear up to 262144 cores, the maximum number tested. The elliptical problems encountered when simulating the Euler equations (velocity projection or calculation of the vector potential) are more difficult to parallelize than the hyperbolic advection term due to their inherent non-local nature. For each timestep, information travels only fractions of the grid spacing in the advection step, but through the whole domain when enforcing the incompressibility. This behavior is necessarily reflected by the demands on communication between processes in massively parallel simulations. With inclusion of the multigrid algorithm, the scaling is efficient only up to 131072 cores.

4.2. Evolution of the flow

This section is devoted to the visible results of the actual simulation of the presented vortex dodecapole configurations. For this purpose, the CWENO vector potential formulation is used in conjunction with adaptively refined meshes for simulations with a resolutions of up to 8192^3 effective grid points, taking into account the increase in resolution due to the high symmetry of the initial conditions. Both the Lamb-dodecapole and the vortex dodecapole are used as initial conditions.

4.2.1. Vortex dodecapole

The vortex dodecapole was chosen as a prototype for the class of vortex dodecapole initial conditions. Its main features are a smooth vorticity profile with compact support and straight, unperturbed initial vortex tubes.

Pictured in Fig. 10 is the evolution in time for the vortex dodecapole initial conditions. Shown are isosurfaces of the absolute vorticity $|\omega(\mathbf{x}, t)|$ at 75% of the peak vorticity for different times. Due to the high symmetry, only one octant of the computational domain is simulated. The figures therefore depict only one half of a vortex tube, with twelve similar tubes in the total domain. The initial phase of the development is depicted in the first two sub-figures: The initially straight tube gets slightly stretched due to interaction with the neighboring tubes. In the third frame, the well-known flattening is in progress. The last three pictures present the final stage of the flow, where the tip of the sheet rolls up and forms a secondary vortex sheet. In the final figure, the secondary sheet exceeds the original sheet in length. Its tip gets drawn out of the collapsing region.

The appearance of the roll-up and the secondary vortex sheet are a first evidence against a locally self-similar amplification and collapse to a point: The initially round vortex tubes are severely deformed and do not resemble their initial configuration in shape. Furthermore, the possibility that the formation of a roll-up may lead to the emergence of a tube-like structure which again form a dodecapole arrangement is clearly conflicting the numerical evidence.

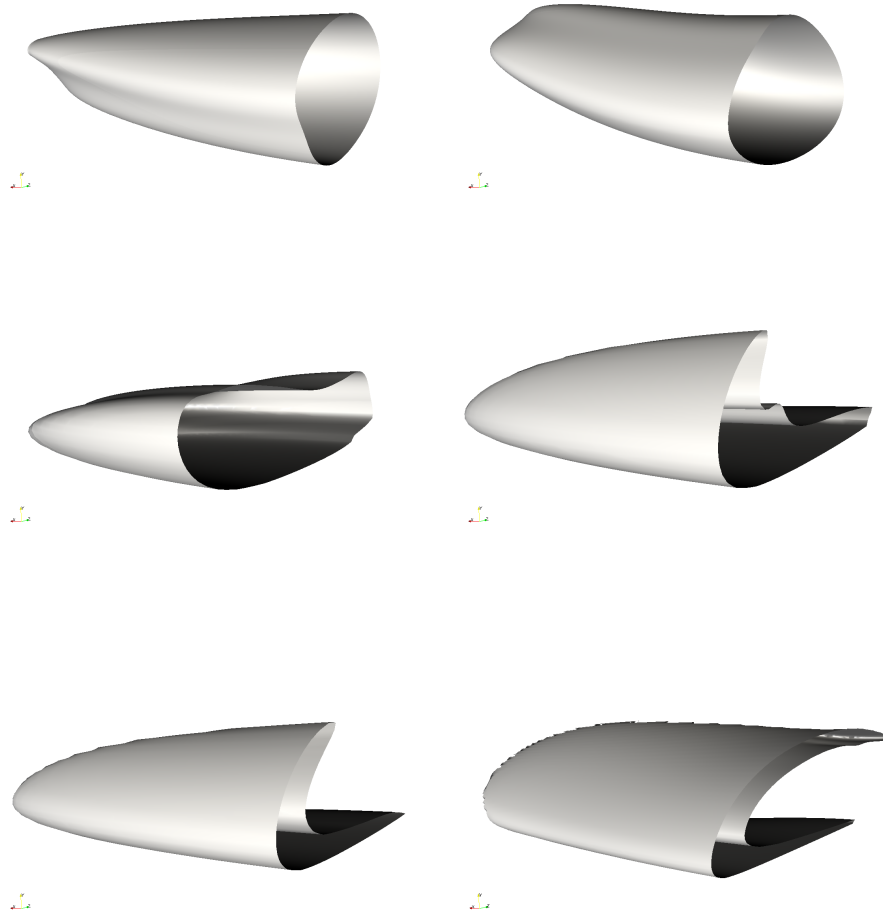


Figure 10: Evolution of the vortex dodecapole. Pictured are isosurfaces of the absolute vorticity, $|\omega(x,t)|$ at 75% of the peak vorticity. Only one of twelve tubes is shown. The flattening of the vortex tube is followed by a roll-up. The developing secondary sheet finally exceeds the original sheet in size. All pictures are from run `amr1`.

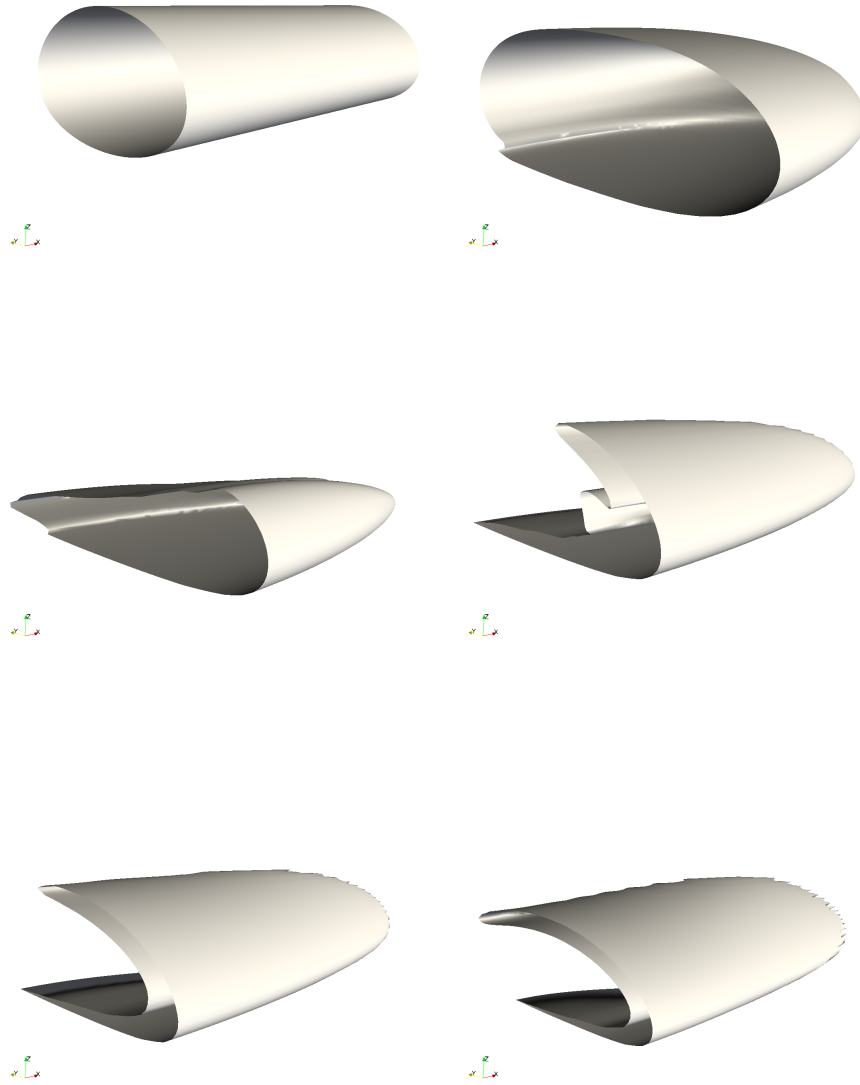


Figure 11: Evolution of the Lamb dodecapole. Pictured are isosurfaces of the absolute vorticity, $|\boldsymbol{\omega}(x, t)|$ at 75% of the peak vorticity. Again, only one of twelve tubes is shown. As before, the vortex tube is flattens, followed by a roll-up. A secondary vortex sheet develops and gets drawn out of the center region. All pictures are from run `lamb`.

4.2.2. Lamb dodecapole

The Lamb dodecapole initial conditions are motivated by the fact that each Lamb dipole in itself is an exact and invariant solution to the Euler equations. It was therefore anticipated in [41] that a more complex setup consisting of Lamb dipoles will exhibit considerably less core deformation for the vortex tubes. If this assumption would be met, the dodecapole arrangement could lead to the formation of a locally self-similar blowup scenario: The Lamb-dipoles would approach and amplify each other, but, without core deformation, stay in their relative alignment and shape. The ever-decreasing length-scale would result in a point-wise collapse to the origin.

As shown in Fig. 11, this scenario is not observed in the numerical simulation. The initial tubes are deformed severely in the course of the simulation. Vortex core deformation is not prevented. This is hardly surprising, since the vortex dodecapole relies on strain imposed by the rotational images of the tube *by design*, while the Lamb dipole configuration only prevents deformation by the reflectional image. Due to the initially close proximity of all twelve vortex tubes and the short timescale of the evolution, deformation induced by the reflectional partner seems to be negligible, regardless of the actual vorticity profile of the tubes.

Altogether, the evolution of the vortex tubes for the Lamb case resembles the above presented vortex dodecapole flow: An initial flattening of the tubes is followed by a roll-up. The emerging secondary vortex sheet gets drawn out and finally exceeds the original sheet in length. Due to the overall similarity of both flows it seems safe to deduce that the topological flow evolution only weakly depends on the precise vorticity profile. This may be seen as motivation to transfer the results for just one particular initial condition to the whole class of vortex dodecapole flows.

4.2.3. Comparison and conclusion

The results of the previous two sections lead to the conclusion that no remarkable differences exist in the overall properties of the flow. In Fig. 12, a direct comparison between low resolution runs (1024^3) for the simple and the Lamb vorticity profile are shown for a late time to reveal the details of the differences. Most of the large-scale structures are identical for both flows. The initial shape of the Lamb profile is responsible for the formation of a less sharp roll-up of the vortex sheet and the accumulation of secondary vorticity inside the kink. Furthermore, the trailing vortex sheet, which is an artifact of the collapse of the vortex dipoles to the center, is considerably stronger for the Lamb dipoles.

Since, additionally, the core deformation is not effectively prevented in the Lamb case, these arguments were the reason that all high resolution runs and all geometric diagnostics were performed for the simple, smooth dodecapole initial conditions.

4.3. Accumulation of vorticity and strain

The vortex dodecapole is designed to be a violent initial condition with rapid accumulation of vorticity. Unlike e.g. the Taylor-Green vortex or Kerr's initial

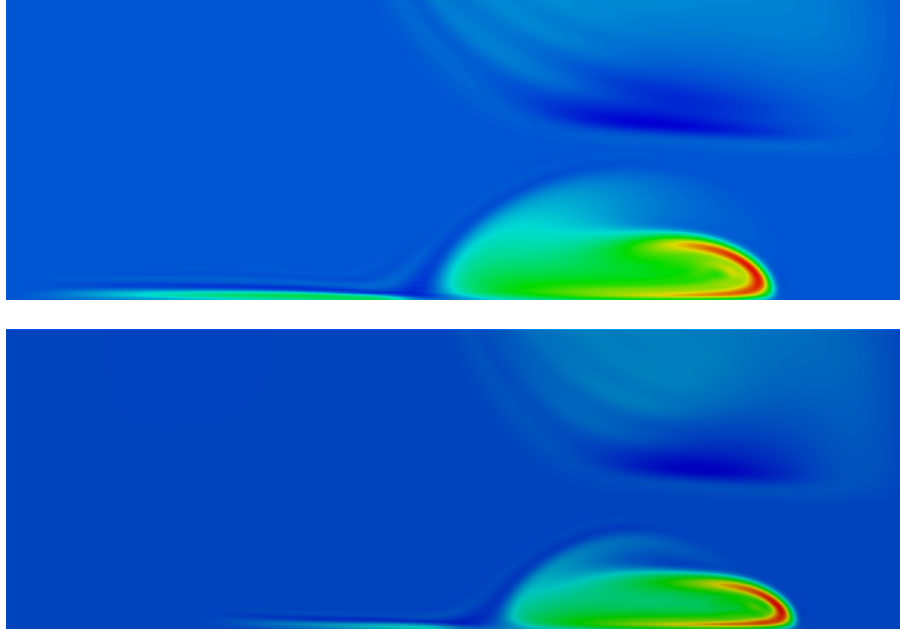


Figure 12: Direct comparison between the Lamb and the simple vorticity profile at late time. The vorticity in a slice near the plane of symmetry, $z = 0.1$, is pictured. The Lamb dodecapole (top) exhibits a more pronounced trailing vortex sheet near the symmetry plane. This effect is considerably smaller for the simple vorticity profile (bottom).

conditions, no sustained phase of flow evolution has to be awaited for the critical structures to form. Thus, vorticity accumulation sets in immediately.

The overall vorticity amplification from initially $\Omega(0) = 20$ to finally $\Omega(t) > 10^5$ exceeds a factor of 500. The location of the maximum vorticity follows the tip of the vortex sheet shown above, and is located at the intersection of the vortex sheets when the roll-up begins to form. The growth of the maximum of the norm of the strain, $\|S(\cdot, t)\|_{L^\infty}$ behaves in a similar manner as the peak vorticity, which is about $\|S(\cdot, 0)\|_{L^\infty} \approx 12.4$ initially and grows by more than two orders of magnitude in the course of the simulation.

The BKM-criterion implies that the growth in time of $\Omega(t)$ has to fulfill $\Omega(t) \approx 1/(T-t)^\gamma$ with $\gamma \geq 1$ to be compatible with a finite-time singularity. A plot of $1/\Omega(t)$ (by assuming $\gamma = 1$) is pictured in Fig. 13. At small times t , this graph looks straight, but the growth rate changes at least twice in the evolution of the flow. This can be explained by competing maxima in $|\omega|$ overtaking the original $\Omega(t)$, thus changing the growth rate at different stages. Nevertheless, at no time the vorticity looks as though saturating, and in the latest stage of development suggests a blowup time of $T \approx 0.72$.

Numerical data of this kind has been interpreted as evidence in favor of the formation of a finite-time singularity before. Yet, even though the plot 13 is rather suggestive, the growth may as well be fitted to some fast (double)

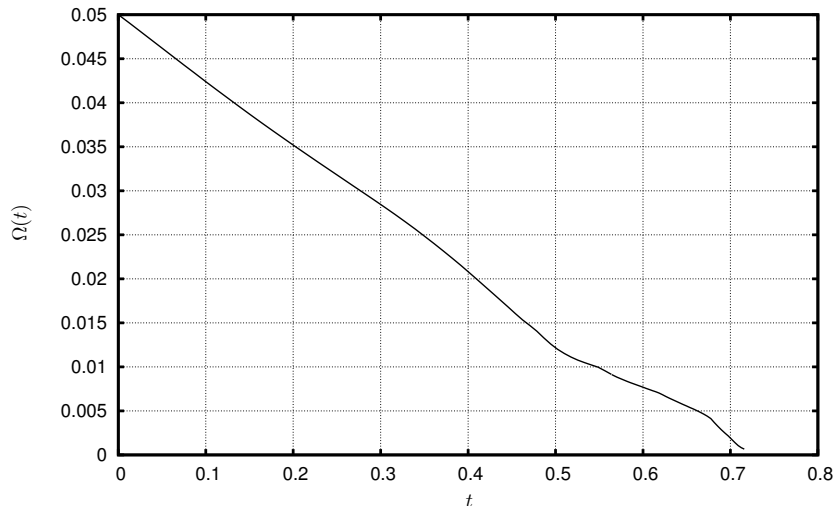


Figure 13: Evolution of $1/\Omega(t)$ in time. This mode of plotting suggests a growth of $\Omega(t) \approx 1/(T-t)^\gamma$ with $\gamma = 1$ and a blowup time $T \approx 0.72$.

exponential growth.

4.4. Geometry of the critical vortex line

It was stated by theorem 1 of [19] that a blowup of vorticity in any point \mathbf{x} is impossible as long as for some \mathbf{y} on the same vortex line uncritical growth of vorticity is observed and along the vortex line connecting \mathbf{x} to \mathbf{y} the integral of $\nabla \cdot \boldsymbol{\xi}$ remains bounded. As lined out above, we re-interpreted this statement as: Supposing there is singular behavior of the maximum vorticity $\Omega(t)$, does the flow allow for a point-wise blowup or is there a blowup of a finite, non-vanishing vortex line segment?

Numerically, this test was implemented as follows:

- At each timestep, identify the point of maximum vorticity as $\mathbf{x}(t)$.
- Follow the vorticity direction vector field while integrating $\nabla \cdot \boldsymbol{\xi}$ along the path. This is done with a third-order Runge-Kutta integrator in space.
- As soon as the integrated quantity exceeds the threshold C , identify the current location on the vortex line as $\mathbf{y}(t)$. To increase precision, the endpoint is found via bisection.
- Geometric properties and diagnostics for the vortex line segment are calculated, especially its length and $|\boldsymbol{\omega}(\mathbf{y}(t), t)|$ to distinguish the cases introduced above.

This procedure is carried out for the whole time interval, as long as the simulation is well resolved. The constant C is chosen in a reasonable way to achieve

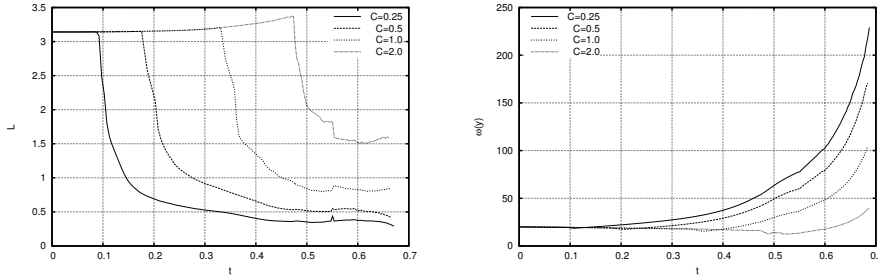


Figure 14: Left: Length of the vortex lines starting at position \mathbf{x} of maximum vorticity for constant $C = \int_x^y \nabla \cdot \xi ds$. Right: Vorticity at the endpoint y of these vortex line. Once satiated, the growth rate is the same for all y .

a length of the vortex line segment that fits into the computational domain in the beginning of the simulation, but is still well resolved at the chosen resolution at later times. Hence, the whole vortex line segment is resolved reliably throughout the simulation.

The results for the vortex dodecapole initial conditions are presented in Fig. 14 for different constants $C \in \{0.25, 0.5, 1, 2\}$. Initially, the vortex line segments do not accumulate enough $\nabla \cdot \xi$, so that the length is bounded by the size of the computational domain ($\mathbf{x} \in [0, \pi]^3$). At some point, depending on the value of C , the threshold is reached and the length of the vortex line segment decreases. Yet, for all considered cases of C , the length does not collapse to a point, but saturates at early times without approaching $l(t) = 0$. This behavior appears to be stable up to the latest time of the simulation. The final length of the vortex line segments is at least 0.3 for the smallest case of C ($C = 0.25$), which is still well resolved with at least $200 \Delta x$. This result, therefore, is a numerical evidence against a point-wise blowup for the vortex dodecapole class of initial conditions. This is in concordance with the estimate in [19].

Monitoring the development of $\omega(\mathbf{y}(t), t)$ yields, as shown in Fig. 14 (right), a similar growth rate for the accumulation of vorticity at the endpoint as for the beginning of the vortex line segment. This is hardly surprising, since by construction a constant value for C directly links the growth rates of $|\omega(\mathbf{x}(t), t)|$ to $|\omega(\mathbf{y}(t), t)|$. Nevertheless, a numerical verification of this analytic equality may be seen as a confirmation that the observed growth rate of $|\omega(\mathbf{x}(t), t)|$ is by no means a numerical artifact in an isolated small area, but is reproduced at points far away from the critical region, which appear to be well-behaved at first view. The possibly critical growth in the perspective of BKM is, thus, confirmed by the global flow.

Furthermore, since for a large portion of the simulation the distance $l(t)$ is approximately constant, this could possibly be seen as an evidence for the existence of a non-vanishing vortex line segment that blows up in every point. The popular scenario of a collapse to a single point, on the other hand, is clearly conflicting the numerical evidence. The discovery of a possibly critical vortex line segment in the vortex dodecapole flow, however, is to be handled with

care, since distinguishing between critical and sub-critical blowup of the whole segment is in no way more conclusive than distinguishing between critical and sub-critical growth of $\Omega(t)$. Thus, learning from the lesson taught by 25 years of numerically testing BKM, this should not be interpreted as clear evidence in favor of a finite-time singularity.

4.5. Lagrangian evolution of the critical vortex line segments

The geometric properties of Lagrangian vortex line segments, especially their curvature κ and the tightening of their surroundings $\nabla \cdot \boldsymbol{\xi}$ have been established as revealing parameters in understanding the nature of rapid accumulation of vorticity in Euler flows and a sound connection to singular behavior is made through theorem 2. The ambition here is to utilize these geometric properties, monitored in a numerical simulation, as more reliable means of distinguishing between a finite-time singularity and a mere fast accumulation of vorticity.

Despite high hopes from an analytical point of view that these considerations will shed light on the nature of vorticity accumulation, numerical results observing geometrical properties of Lagrangian vortex filaments are scarce. This is primarily due to the fact that Eulerian quantities such as $\Omega(t)$ are readily trackable in post-processing, while monitoring the Lagrangian evolution requires additional computational effort. On top of that, the geometry of integral curves at an instance in time, though in principle computable in post-processing, as well as derived quantities such as their convergence and curvature, are quite inaccessible in comparison to simple Eulerian criteria.

This section is devoted to the presentation of results concerning the assumptions of theorem 2 of [19] for the vortex dodecapole initial conditions. Quite similar to the first theorem, there is considerable freedom in the choice of the involved quantities. The strategy we chose in the context of this paper is as follows:

- Identify the Lagrangian fluid element $\boldsymbol{\alpha}$, which will contain the maximum of vorticity at the latest time of the simulation, $\Omega(t) \approx |\boldsymbol{\omega}(\mathbf{X}(\boldsymbol{\alpha}, t), t)|$. A vortex line segment L_t starting here will intrinsically be “comparable” to the maximum of vorticity (as in $|\boldsymbol{\omega}(\mathbf{X}(\boldsymbol{\alpha}, t), t)| \gtrsim \Omega(t)$) at late stages of the simulation. The assumptions concerning the segment are therefore automatically met. In the numerics this procedure is implemented by carrying out a precursory identical simulation with a huge number of tracer particles (≈ 1 million) randomly distributed across the domain. Particles that accumulate huge amounts of vorticity are selected for the subsequent production run.
- For the production run, at each instance in time start a vortex line integration at $\mathbf{X}(\boldsymbol{\alpha}, t)$ along the vorticity direction field. Monitor the maximum curvature $\|\kappa\|_{L^\infty(L_t)}$ and the maximum vortex line convergence $\|\nabla \cdot \boldsymbol{\xi}\|_{L^\infty(L_t)}$ during the integration and calculate $\lambda(t)$. Stop the integration, as soon as $\lambda(t)$ reaches a fixed, arbitrary constant C . This defines L_t . In the numerics this is again implemented with a third-order Runge-Kutta integration and bisectioning to obtain the endpoint of L_t .

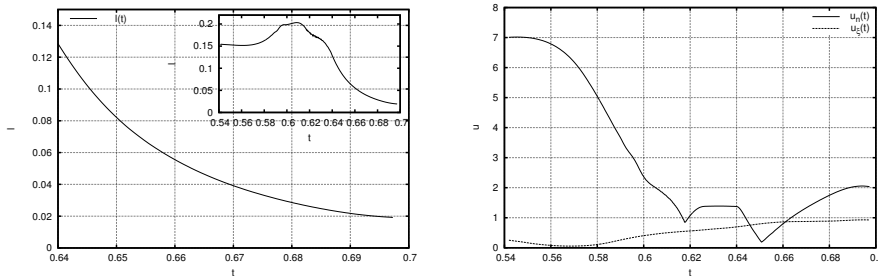


Figure 15: Top: Evolution of the length $l(t)$ of the critical vortex filament L_t for different Lagrangian fluid elements. The length does not decrease as $(T - t)^B$ for any $B < 1$, which would be faster than linear. The Lagrangian collapse of the vortex segment is decelerating instead. Bottom: Evolution of the quantities U_n and U_ξ in time. U_n does not appear to be growing, while U_ξ , though increasing in time, does not exhibit a finite-time blowup as $1/(T - t)$.

- For this vortex line segment L_t , calculate the length $l(t)$, and the velocity components U_n and U_ξ . From the collapse of the length $l(t)$ approximate the exponent B . This in turn provides the critical growth exponent A for the velocity variables, $A_{\text{crit}} = 1 - B$.
- Compare the increase in U_n and U_ξ to $1/(T - t)^{A_{\text{crit}}}$ to distinguish between critical and sub-critical growth of velocity.

This can be interpreted rather intuitively. By prescribing an arbitrarily fixed $\lambda(t)$, the vortex line segment is kept relatively geometrically uncritical, as the length-scale is always adjusted accordingly. This process of “zooming in” just enough to retain the geometric “criticalness” prescribes the rate of collapse to a point, at least in the direction of the vortex line. All that is left to check is whether the velocity growth in the immediate surrounding is fast enough to be compatible with a finite-time singularity.

The results of the previous section, concerning a point-wise singularity versus the blowup of a whole vortex segment, already anticipates that the increase in $\nabla \cdot \xi$ around the critical vortex line is bounded. If the curvature of the vortex line segment remains controllable (which is to be expected from the pictures), then just a mild collapse of $l(t)$ occurs. This leaves much room for U_n and U_ξ to still be distinguishable from a critical growth.

Fig. 15 shows the results for the vortex dodecapole initial conditions for a fixed constant C . Different choices of the constant C produce identical, rescaled results. The top plot pictures the length of the vortex line segment for the tracer that is arriving at a position of very huge vorticity at late stages of the simulation. The subplot depicts the long-term behavior of the particle entering the critical region, while the final stage of length decrease is magnified. The decrease in length does not agree with a collapse in final time, but instead the shrinkage of the segment decelerates clearly in time. This contradicts a scaling in time proportional to $(T - t)^B$ for any $0 < B \leq 1$, which would be faster than (or, in the limiting case, equal to) linear. It should be noted that for the

observed collapse in length, the vortex segment curvature κ is the dominating term in $M(t) = \max(\|\nabla \cdot \boldsymbol{\xi}\|_{L^\infty(L_t)}, \|\kappa\|_{L^\infty(L_t)})$, shadowing the effects of $\nabla \cdot \boldsymbol{\xi}$. This may lead to a change of regime in the rate of collapse, if $\nabla \cdot \boldsymbol{\xi}$ at some point exceeds κ in quantity.

It could furthermore be argued that the limit $B \rightarrow 0$ is hard to exclude, since the drop in length would be virtually instantaneous in time, with a close to constant scaling before. In this limit, the quantities U_n and U_ξ would have to grow roughly as $1/(T-t)$ to still allow formation of a finite-time singularity. U_ξ quantifies the largest difference in axial velocity along the segment. For an isolated collapsing vortex tube, this quantity can be expected to not increase critically, since the tangential velocity is less likely to rapidly change than the radial velocity. However, this initial explanation does not consider the influence of the mirror tubes. U_n on the other hand may be interpreted as the velocity of the vortex tube's core itself. Again, in an isolated setup this velocity is not expected to blow up.

Fig. 15 (bottom) shows the observed behavior of U_n and U_ξ in time for the tracer as considered above. U_n stays roughly constant in time, showing no signs of a blowup. U_ξ , even though increasing in time, does not fit to critical growth, in particular not like $1/(T-t)$ in time. Thus, the assumptions of theorem 2 are well met. This result therefore poses a strong numerical evidence against a finite-time singularity for the class of vortex dodecapole initial conditions.

5. Conclusion

In this paper we present numerical evidence against the formation of a finite-time singularity for the vortex dodecapole initial condition. We use data obtained from high resolution adaptively refined numerical simulations to test the assumptions presented by geometric blowup criteria. The applied numerical method allows for a clearer insight into the formation of the possible singularity. Most notably, it implies numerical techniques to distinguish between a point-wise blowup and the blowup of a whole vortex line segment. Furthermore, by tracking curvature and spreading of Lagrangian vortex line segments, the distinction between singular and non-singular behavior can be made much more clearly than the usual approach via BKM.

In this paper we used vortex dodecapole initial conditions with two different vorticity profiles. Comparison of the simulation shows that different vorticity profiles yield similar visual and geometrical appearance. This serves as an argument that the obtained results may apply to the whole class of vortex dodecapole flows. Monitoring the growth rate of $\Omega(t)$ quantifies the well-known vorticity amplification. Amplification by more than two orders of magnitude was reached for both vorticity and strain, exceeding by far values achieved by previous simulations [40]. Applying this data to BKM would lead to the conclusion that a finite-time singularity at time $T \approx 0.72$ fits via extrapolation. Yet, as the history of Euler simulations has shown, statements obtained by extrapolation are to be handled with care.

Following the presented argument, a point-wise collapse should coincide with a blowup of $\nabla \cdot \xi$ at the point of maximum vorticity. As shown, this statement can be broadened: A finite-time singularity must either lead to a blowup of $\nabla \cdot \xi$ at the point of maximum vorticity, or the whole critical vortex line segment has to blow up. Utilizing the geometric information obtained via vortex line integration from the numerical simulation, it is observed that $\nabla \cdot \xi$ does not grow in a way to be compatible with a point-wise collapse. Yet, measuring the growth-rates on the critical vortex line, high rates of amplification are measured far away from the critical region. Even though it is hard to distinguish, whether this amplification is critical or sub-critical, this might be interpreted as an evidence for the blowup of the complete vortex line segment, even though it suffers exactly the same vulnerabilities as extrapolation in BKM. A point-wise blowup, on the other hand, clearly contradicts the numerical results up to the time reached.

Evidence against a blowup of the whole critical vortex line segment is found when looking at the geometric properties of Lagrangian vortex line segments. It was shown by theorem 2 in [19] that a blowup of vorticity is directly connected to the interplay between velocity growth and the collapse of vortex line filaments, when maintaining the overall same shape in geometric means (i.e. the same $\lambda(L_t)$). Since curvature and $\nabla \cdot \xi$ do not increase in order to support a finite-time collapse of the segment, velocity components in the vicinity of the vortex line filament would have to increase as $1/(T - t)$ to support the blowup hypothesis. Up to the time reached, this critical velocity growth may be excluded by numerical means. This poses a numerical evidence against the formation of a singularity in finite time for vortex dodecapole configurations.

Acknowledgment

We would like to thank J. Dreher for his work on the computational framework. This work benefited from support through project GR 967/3-1 of the Deutsche Forschungsgesellschaft. Access to the BlueGene/P multiprocessor computer JUGENE at the Forschungszentrum Jülich was made available through project hbo35.

References

- [1] C. Fefferman, Existence and smoothness of the Navier-Stokes equation, published online:
<http://www.claymath.org/millennium/> (2000).
- [2] O. A. Ladyzhenskaya, Sixth problem of the millenium: Navier-Stokes equations, existence and smoothness, *Russian Math. Surveys* 58 (2001) 251–286.
- [3] C. R. Doering, The 3D Navier-Stokes problem, *Annual Review of Fluid Mechanics* 41 (2009) 109–128.

- [4] L. Caffarelli, R. Kohn, L. Nirenberg, Partial regularity of suitable weak solutions of the Navier-Stokes equations, *Comm. Appl. Math.* 35 (1982) 771–831.
- [5] J. Leray, Sur le mouvement d’un liquide visqueux emplissant l’espace, *Acta Math.* 63 (1934) 193–248.
- [6] P. Constantin, On the Euler equations of incompressible fluids, *Bulletin Amer. Math. Soc.* 44 (4) (2007) 603–621.
- [7] Z. She, E. Lévêque, Universal scaling laws in fully developed turbulence, *Physical Review Letters* 72 (3) (1994) 336–339.
- [8] U. Frisch, *Turbulence*, Cambridge University Press, Cambridge, 1995.
- [9] A. N. Kolmogorov, Local structure of turbulence in an incompressible fluid at very high Reynolds numbers, *Dokl. Akad. Nauk SSSR* 30 (1941) 299–303.
- [10] A. N. Kolmogorov, Energy dissipation in locally isotropic turbulence, *Dokl. Akad. Nauk SSSR* 32 (1941) 19–21.
- [11] A. N. Kolmogorov, A refinement of previous hypotheses concerning the local structure of turbulence in a viscous incompressible fluid at high Reynolds numbers, *J. Fluid Mech.* 13 (1962) 82–85.
- [12] L. Onsager, Statistical hydrodynamics, *Nuovo Cimento (Supplemento)* 6 (1949) 279–287.
- [13] P. Constantin, W. E, E. S. Titi, Onsager’s conjecture on the energy conservation for solutions of Euler’s equation, *Commun. Math. Phys.* 165 (1994) 207–209.
- [14] A. Cheskidov, P. Constantin, S. Friedlander, R. Shvydkoy, Energy conservation and Onsager’s conjecture for the Euler equations, *Nonlinearity* 21 (6) (2008) 1233.
- [15] J. D. Gibbon, The three-dimensional Euler equations: Where do we stand?, *Physica D: Nonlinear Phenomena* 237 (2008) 1894–1904.
- [16] J. T. Beale, T. Kato, A. Majda, Remarks on the breakdown of smooth solutions for the 3-D Euler equations, *Commun. Math. Phys.* 94 (1984) 61–66.
- [17] P. Constantin, C. Fefferman, A. Majda, Geometric constraints on potentially singular solutions for the 3D Euler equations, *Commun. Part. Diff. Eq.* 21 (1996) 559–571.
- [18] D. Cordoba, C. Fefferman, On the collapse of tubes carried by 3D incompressible flows, *Commun. Math. Phys.* 222 (2001) 293–298.

- [19] J. Deng, T. Y. Hou, X. Yu, Geometric properties and nonblowup of 3D incompressible Euler flow, *Commun. Part. Diff. Eq.* 30 (1-2) (2005) 225–243.
- [20] P. Constantin, Geometric statistics in turbulence, *SIAM Rev.* 36.
- [21] J. D. Gibbon, A quaternionic structure in the three-dimensional Euler and ideal magneto-hydrodynamics equation, *Physica D: Nonlinear Phenomena* 166 (17).
- [22] J. D. Gibbon, D. D. Holm, R. M. Kerr, I. Roulstone, Quaternions and particle dynamics in Euler fluid flow, *Nonlinearity* 19 (1969).
- [23] J. Deng, T. Y. Hou, X. Yu, Improved geometric conditions for non-blowup of the 3D incompressible Euler equation, *Commun. Part. Diff. Eq.* 31 (2) (2006) 293–306.
- [24] W. T. Ashurst, A. R. Kerstein, R. M. Kerr, C. H. Gibson, Alignment of vorticity and scalar gradient with strain rate in simulated NavierStokes turbulence, *Phys. Fluids* 30 (1987) 2343.
- [25] C. Meneveau, Lagrangian dynamics and models of the velocity gradient tensor in turbulent flows, *Annual Review of Fluid Mechanics* 43 (2011) 219–245.
- [26] L. Chevillard, C. Meneveau, Lagrangian time correlations of vorticity alignments in isotropic turbulence: Observations and model predictions, *Phys. Fluids* 23.
- [27] A. Pumir, E. Siggia, Collapsing solutions to the 3-D Euler equations, *Phys. Fluids A* 2 (2) (1990) 220–241.
- [28] P. E. Hamlington, J. Schumacher, W. J. A. Dahm, Direct assessment of vorticity alignment with local and nonlocal strain rates in turbulent flows, *Phys. Fluids* 20.
- [29] G. I. Taylor, A. E. Green, Mechanism of the production of small eddies from large ones, *Proc. R. Soc. Lond. A* 158 (1937) 499–521.
- [30] R. M. Kerr, Evidence for a singularity of the three-dimensional, incompressible Euler equations, *Phys. Fluids A* 5 (7) (1993) 1725–1746.
- [31] R. M. Kerr, Velocity and scaling of collapsing Euler vortices, *Phys. Fluids* 17.
- [32] T. Y. Hou, R. Li, Dynamic depletion of vortex stretching and non-blowup of the 3-D incompressible Euler equations, *Journal of Nonlinear Science* 16 (2006) 639–664.
- [33] R. B. Pelz, Symmetry and the hydrodynamic blow-up problem, *J. Fluid Mech.* 444 (2001) 299–320.

- [34] S. Kida, Three-dimensional periodic flows with high symmetry, *J. Phys. Soc. Jpn.* 54 (1985) 2132–2136.
- [35] O. N. Boratav, R. B. Pelz, Evidence for a real-time singularity in hydrodynamics from time series analysis, *Phys. Rev. Lett.* 79 (1994) 4998–5001.
- [36] R. B. Pelz, Extended series analysis of full octahedral flow: numerical evidence for hydrodynamic blowup, *Fluid Dyn. Research* 33 (2003) 207–221.
- [37] C. Cichowlas, M. Brachet, Evolution of complex singularities in Kida-Pelz and Taylor-Green inviscid flows, *Fluid Dyn. Research* 36 (2005) 239–248.
- [38] C. S. Ng, A. Bhattacharjee, Sufficient condition for a finite-time singularity in a high-symmetry Euler flow: Analysis and statistics, *Phys. Rev. E* 54 (1996) 1530–1534.
- [39] O. N. Boratav, R. B. Pelz, Direct numerical simulation of transition to turbulence from a high-symmetry initial condition, *Phys. Fluids* 6 (8) (1994) 2757–2784.
- [40] T. Grafke, H. Homann, J. Dreher, R. Grauer, Numerical simulations of possible finite time singularities in the incompressible Euler equations: comparison of numerical methods, *Physica D: Nonlinear Phenomena* 237 (2008) 1932–1936.
- [41] P. Orlandi, G. F. Carnevale, Nonlinear amplification of vorticity in inviscid interaction of orthogonal Lamb dipoles, *Phys. Fluids* 19.
- [42] H. Lamb, *Hydrodynamics*, Cambridge University Press, 1932.
- [43] J.-Z. Wu, H.-Y. Ma, M.-D. Zhou, *Vorticity and Vortex Dynamics*, Springer, 2006.
- [44] U. Frisch, T. Matsumoto, J. Bec, Singularities of Euler flow? Not out of the blue!, *J. Stat. Phys.* 113 (2003) 761–781.
- [45] R. H. Morf, S. A. Orszag, U. Frisch, Spontaneous singularity in three-dimensional, inviscid, incompressible flow, *Physical Review Letters* 44 (9) (1980) 572–575.
- [46] A. J. Chorin, Estimates of intermittency, spectra, and blow-up in developed turbulence, *Communications on Pure and Applied Mathematics* 34 (6) (1981) 853–866.
- [47] A. J. Chorin, The evolution of a turbulent vortex, *Commun. Math. Phys.* 83 (1982) 517–535.
- [48] E. D. Siggia, Collapse and amplification of a vortex filament, *Phys. Fluids* 28 (1985) 794–805.

- [49] J. B. Bell, D. L. Marcus, Vorticity intensification and transition to turbulence in three-dimensional Euler equations, *Commun. Math. Phys.* 147 (1992) 371–394.
- [50] M. E. Brachet, D. I. Meiron, S. A. Orszag, B. G. Nickel, R. H. Morf, U. Frisch, Small-scale structure of the Taylor-Green vortex, *J. Fluid Mech.* 130 (1983) 411–452.
- [51] M. E. Brachet, M. Meneguzzi, A. Vincent, H. Politano, P. L. Sulem, Numerical evidence of smooth self-similar dynamics and possibility of subsequent collapse for three-dimensional ideal flows, *Phys. Fluids* 4 (12) (1992) 2845–2854.
- [52] R. Grauer, C. Marliani, K. Germaschewski, Adaptive mesh refinement for singular solutions of the incompressible Euler equations, *Physical Review Letters* 80 (19) (1999) 4177–4180.
- [53] M. D. Bustamante, M. Brachet, On the interplay between the BKM theorem and the analyticity-strip method to investigate numerically the incompressible Euler singularity problem, published online, <http://arxiv.org/abs/1112.1571> (2011).
- [54] J. Dreher, R. Grauer, Racoon: A parallel mesh-adaptive framework for hyperbolic conservation laws, *Parallel Computing* (2005) 913–932.
- [55] C. Shu, S. Osher, Efficient implementation of essentially non-oscillatory shock-capturing schemes, *Journal of Computational Physics* 77 (1988) 439–471.
- [56] A. Kurganov, D. Levy, A third-order semidiscrete central scheme for conservation laws and convection-diffusion equation., *Jour. Sci. Comp.* 22 (4) (2000) 1461–1488.